RESEARCH ARTICLE

Super-elastic Scintillating Fibers and Fabrics for Efficient and Visual Radiation Detection

Minghui Du[1,2] · Jin Wang[3] · Sijia Xu[4] · Hongwei Li[1,5] · Zhihao Zhang[1,5] · Yankun Qi[1,5] · Shichao Lv[1,5] · Jianrong Qiu[6] · Yurong Yan[4] · Shifeng Zhou[1,5]

Abstract

The fabrication of advanced radiation detectors is an important subject due to the wide use of radiation sources in scientific instruments, medical services, security check, non-destructive inspection, and nuclear industries. However, the manufacture of flexible and stretchable radiation detectors remains a challenge. Here, we report the scalable fabrication of super-elastic scintillating fibers and fabrics for visual radiation detection by thermal drawing and melt-spinning methods using styrene-b-(ethylene-co-butylene)-b-styrene, and scintillating Gd_2O_2S: Tb (GOS). Microstructure evolution, rheological properties, and radiation–composite interaction are studied to reveal the excellent processability, elasticity, and radiation detection ability of the fabricated fibers. Benefiting from the physical crosslinking structural features of the polymer matrix and the excellent radiation absorption capacities of GOS, the resulting fiber can sustain high strains of 765% with a high content of GOS dopants (2 wt.%) and has excellent X-ray detection performance with the limit down to 53 $nGy_{air}\,s^{-1}$. Furthermore, stretchable fabrics are constructed, and their applications in various fields, such as radiation warning, and X-ray imaging, are demonstrated. Our work not only provides a new type of super-elastic scintillating fibers and fabrics for smart textiles but also demonstrates their potential applications in the nuclear field.

Keywords Elastic fiber · Radiation detection · Optical materials · X-ray imaging

Introduction

Radiation detection has attracted wide attention in recent years due to the extensive use of radiation sources in various fields, such as scientific instruments, medical services, security check, non-destructive inspection, and nuclear industries [1–5]. These high-energy radiation sources can not only release free electrons and characteristic rays, but also trigger physical processes such as photolysis, luminescence, and ionization [6]. On the basis of these physical processes, various radiation detectors, such as semiconductor detectors, scintillation counters, photographic plates, and

Minghui Du and Jin Wang have contributed equally to this work.

✉ Shichao Lv
lvshichao@scut.edu.cn

✉ Yurong Yan
yryan@scut.edu.cn

✉ Shifeng Zhou
zhoushifeng@scut.edu.cn

[1] State Key Laboratory of Luminescent Materials and Devices, School of Materials Science and Engineering, South China University of Technology, Guangzhou 510641, China

[2] Institute of Photonics Technology, Jinan University, Guangzhou 510632, China

[3] National Engineering Research Center of Novel Equipment for Polymer Processing, School of Mechanical and Automotive Engineering, South China University of Technology, Guangzhou 510641, China

[4] Key Lab Guangdong High Property & Functional Polymer Materials, School of Materials Science and Engineering, South China University of Technology, Guangzhou 510641, China

[5] Guangdong Provincial Key Laboratory of Fiber Laser Materials and Applied Techniques, Guangdong Engineering Technology Research and Development Center of Special Optical Fiber Materials and Devices, Guangzhou 510641, China

[6] College of Optical Science and Engineering, State Key Laboratory of Modern Optical Instrumentation, Zhejiang University, Hangzhou 310027, China

ionization gauges, have been developed in the past decades [7–10]. Generally, radiation detectors can be divided into two categories: direct scheme and indirect scheme. Direct radiation detectors, such as semiconductor detector, can directly generate electrical signals when they are irradiated by high-energy rays, i.e., X-ray and γ-ray [11]. The key materials used for direct radiation detectors need to have excellent optoelectronic properties (i.e., high carrier mobility, long carrier lifetime, and low trap density), large atomic coefficients, and good radiation resistance. For example, amorphous Se, PbI_2, HgI_2, TlBr, CdTe, CdZnTe, and various perovskite crystals are widely used in direct radiation detectors [12–15]. Indirect radiation detectors, such as a scintillator, can convert high-energy radiation into visible photons, which are then detected by photoelectric sensors, such as photomultiplier tubes and photodiodes [16–18]. The scintillators must have high light yield, short lifetime, high density, and good stability. The commonly used scintillators can be divided into inorganic and organic scintillators. Inorganic scintillators are usually inorganic crystals, such as $Lu_{1.8}Y_{0.2}SiO_5$: Ce, SrI_2: Eu, NaI: Tl, and ZnS: Ag [19, 20]. The other is vitreous, such as cerium-activated lithium glass [21]. Pure crystals with high density, such as bismuth germinate, cadmium tungstate, and barium fluoride, have also been developed for radiation detection [22–24]. Organic scintillators primarily contain three categories, namely organic crystals, organic liquids, and plastic scintillators. The commonly used organic scintillators are cyclic hydrocarbons, such as anthracene, astragalus, naphthalene, and p-triphenyl [25, 26]. Different kinds of radiation detectors have been developed, and they typically require multiple steps to transform the readout signals into useful information. In addition, these rigid devices are rarely compatible with flexible and wearable devices. Therefore, developing flexible and stretchable radiation detectors that can directly indicate the radiation information with high sensitivity is of great significance.

Fiber-based devices have promising applications in radiation detection due to their unique advantages of high flexibility, one-dimensional form, small size, light weight, and large aspect ratio [27–29]. It can be used in a special environment where it is inaccessible using the conventional flat-panel radiation detectors. Furthermore, fiber detectors enable remote and real-time detection with high sensitivity, and they can be easily woven into large-area of fabrics or two- and three-dimensional complex structures, which have potential applications in various radiation detection scenarios. However, the fabrication and development of flexible and stretchable fibers for radiation detection are still important tasks.

In this work, we report a series of super-elastic fibers and fabrics with visual radiation detection and imaging functions through the scalable thermal drawing and melt-spinning

methods using styrene-*b*-(ethylene-*co*-butylene)-*b*-styrene (SEBS) and scintillating GOS. The optimum assemblies of scintillating activators and thermoplastic elastomer matrix endow the fiber and fabric with excellent stretchability and radiation detection ability, which can sustain strains up to 765% and a low X-ray detection limit of 53 $nGy_{air} s^{-1}$. In addition, the obtained elastic fiber shows superstability, thus being able to withstand 2,000 times of cyclic stretching at a 100% elongation. Stretchable fabrics for visual radiation detection in computed tomography scan, radiation protection, and imaging are also demonstrated. These elastic fibers and fabrics can be potentially developed into a new type of smart textiles, pointing to their promising applications in nuclear-related fields.

Experimental Section

Fabrication of Super-elastic Fibers and Fabrics

Styrene-*b*-(ethylene-*co*-butylene)-*b*-styrene (SEBS, G1657; specific gravity 0.91 g/cm^3) was purchased from Kraton Performance Polymers Inc. Kraton G1657 M is a clear, linear triblock copolymer based on styrene and ethylene/butylene with a polystyrene content of 13%. Polypropylene (PP, H39L; specific gravity 0.92 g/cm^3) was purchased from China National Petroleum Corporation. The scintillators Gd_2O_2S: Tb were purchased from Shanghai Keyan Optoelectronics Co., Ltd.

For the preform preparation, SEBS granules and Gd_2O_2S: Tb were first mixed using an internal mixer for 10 min with a temperature of 170 ℃. Then, the composite was hot-pressed into preforms under a pressure of 8 MPa for 20 min at 190 ℃ using a Meyer press. All the preforms in this work have a width of 16 mm, a length of 20 mm, and a thickness of 5 mm. Finally, the preform was thermally drawn into fibers in a vertical furnace at a temperature of 250 ℃–280 ℃. During the drawing process, the preform feeding speed was 1 mm min^{-1}, and the fiber drawing speed was 1.6 m min^{-1}.

For the fabric fabrication, GOS/SEBS multi-filaments and nonwoven samples with and without blending PP were produced on a Melten Spinning-Nonwoven Bifunctional Equipment HY-2 (Longkou Huada Machinery Engineering Co., Ltd., Shandong, China). A single screw extruder with a diameter of 25 mm, a length-to-diameter ratio of 30, and four-zone control systems was used to melt and pressurize polymers, and the screw extrusion temperatures were graduated between 230 ℃ and 260 ℃. A gear metering pump was used to measure the mass flow rate of 25 g/min, and a spin pressure of 4.5 MPa was used. The polymer molten fluids were extruded through a 60-hole spinneret (diameter of 0.5 mm for each hole) and then cooled in a cooling system with an air temperature of 20 ℃ and a relative humidity of

65%–90%. Then, they were rolled onto a roller at a speed of 80–100 m/min to obtain GOS/SEBS with and without PP blending multi-filaments. GOS/SEBS blended nonwovens with and without PP samples were prepared with polymer molten fluids extruded through the spinneret and then air-drawn in a chamber with a purified air temperature of 30 ℃ and speed of 300 m/min after the webbing and rolling steps. A two-stage-drawn unit was used to fulfill the drawn process of targeted multi-filaments, and the total drawn ratio (DR) varied with the addition ratio of GOS and PP ratio into the SEBS matrix. The ratio of GOS to SEBS varied from 2 to 10% by weight, and the ratio for PP to SEBS was 10%–30% by weight.

Material Characterizations

Optical images of the elastic fibers were captured by a Leica microscope (DM4000, Germany). Scanning electron microscope (SEM) images and elemental mapping were performed on a Merlin SEM (30 kV, BSE Zeiss, Germany). The stress–strain curve of the fibers was measured by an electromechanical universal testing machine (Instron 5967/Z 100, America) with the tensile mode of a 100 N load cell and 200 mm/min test rate. Rheological properties, including the storage modulus, loss modulus, and complex viscosity of the fibers, were measured by a rotational rheometer (Anton Paar MCR 302, Germany). Wide-angle X-ray scattering (WAXS) measurements were performed by a Rigaku system equipped with a Fr-x rotating anode target X-ray source (the maximum output power is 2.97 kW, and the focal spot diameter of electron beam is 70 μm).

X-Ray Detection and Imaging Characterization

A Mini-X-OEM Rh target X-ray tube was used as the excitation source in measuring the X-ray detection performance. The X-ray source was operated with a constant 40 kV acceleration voltage. The X-ray dose rate was controlled by tuning the operational current from 0 to 100 μA and calibrated with a Radcal ion chamber dosimeter. All the measurements were conducted at room temperature.

For X-ray imaging, the radiation detection fabric was placed on the surface of the pen embedded with a metallic spring. A beam of X-rays produced by the Mini-X-ray tube was applied to the pen with different exposure times and dosages. The images were recorded by a digital camera. All the measurements were conducted at room temperature.

Theoretical Simulation

The Monte Carlo method was used to study the interaction between X-ray and the elastic fibers. The radiation matter interaction on the elastic fiber was investigated using GEANT4 software, and the resulting data were analyzed using ROOT. C language was used in setting the X-ray source and fiber model. The parameters of the X-ray source were set in the PrimaryGeneratorAction.cc file. The energy of the X-ray source was set at 40 keV, and the size of the pencil beam was 1.0×1.0 mm^2. The composite structure of the elastic fiber was simplified as homogeneous, and the NIST database was used in defining materials. The fiber size was 0.5×1 mm^2. The energy deposition of the photoelectric effect and the Compton effect was investigated using the default physics lists, which can be selected in GEANT4 by referring to the GEANT4 Physics Reference Manual. The event number of high-energy photons was set at 10^7. The data of energy deposition were collected in StepAction.cc file and processed by ROOT software in RunAction.cc file.

Results and Discussion

Design and Fabrication of Super-elastic Fibers

To develop flexible and stretchable fibers with visual radiation detection function, a thermoplastic polymer matrix that is compatible with the thermal drawing and melt-spinning process needs to be screened first. The tensile modulus of commonly used polymers compatible with the melting process is shown in Fig. 1a. Among these polymers, SEBS ($T_g \approx 120$ ℃, Young's modulus $E = 2.4$ MPa), a linear triblock copolymer with polystyrene as the terminal segment and ethylene–butene copolymer obtained by hydrogenation of polybutadiene as the middle elastic block was selected as the matrix due to its high stretchability, excellent thermoplasticity, UV stability, and aging resistance [30]. The scintillator material GOS was selected as the activator because of its excellent radiation absorption capacities and outstanding luminescent properties, and it is widely used in X-ray imaging and flat-panel detectors [31, 32]. Moreover, GOS has a short luminescence decay time of only 1 ms, which is very sensitive for radiation detection and X-ray imaging.

Once the constituent materials have been identified, the target elastic fibers can be fabricated by a scalable thermal drawing technique, as illustrated in Fig. 1b. This technique starts with the construction of a macroscopic preform, which can be processed into various architectures, such as round and square. Next, the preform was heated in a shaft furnace to a temperature higher than the glass transition temperature (T_g) of the constituent materials, and it can be thermally drawn into kilometer-long fibers under an external pull. During the thermal drawing process, the thickness of the elastic fiber can be monitored in real time by a laser rangefinder, and it ranges from macro- to micro-scale. Generally, the thickness of the final fiber can be rationally controlled by tuning the drawing temperature, the feeding
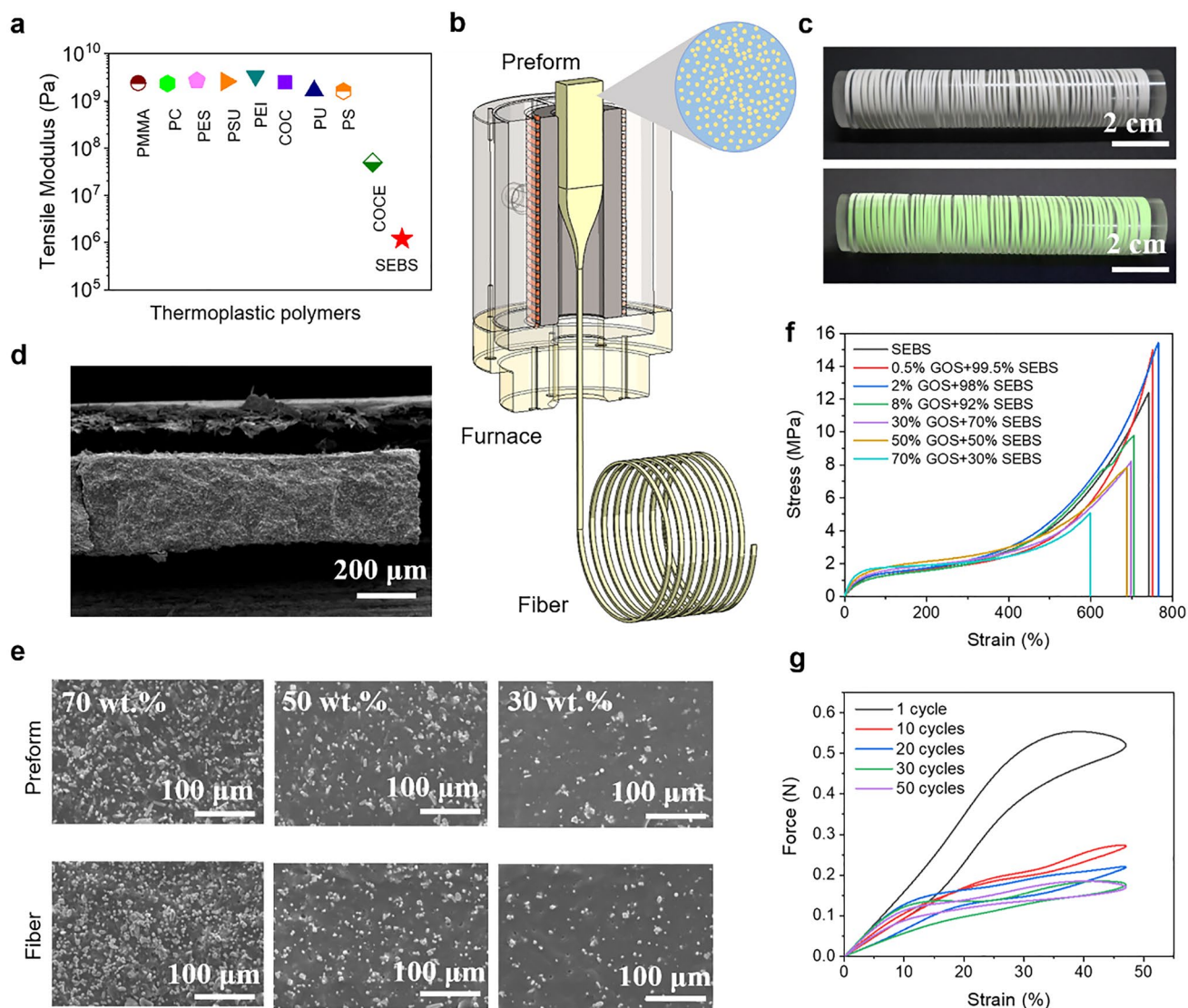
Fig. 1 Fabrication and characterization of the elastic fibers. **a** Tensile modulus of the commonly used polymers, including polymethyl methacrylate (PMMA), polycarbonate (PC), polystyrene (PS), SEBS, polyethersulfone (PES), polysulfone (PSU), polyetherimide (PEI), cycloolefin copolymer (COC), polyurethane (PU), and cyclic olefin copolymer elastomer (COCE). **b** The schematic diagram of the thermal drawing technique. **c** The images showing the drawn elastic fiber rolled up on a PMMA rod, and irradiated by a 254 nm UV light. **d**, **e** Scanning electron microscope (SEM) images of the cross-section of the preform and drawn fiber loaded with 30 wt.%, 50 wt.%, and 70 wt.% GOS, respectively. **f** The stress–strain curves of the drawn elastic fibers loaded with different ratio of GOS. Each sample has tested for more than three times, and the error of stress is ±0.2 MPa. **g** Elastic recovery property of the fiber loaded with 70 wt.% GOS at a 50% elongation

speed of the preform, the drawing speed of the fiber, and the initial diameter of the macroscopic preform. With the use of this simple and scalable technique, a single preform can yield extremely long and uniform fibers with the same cross-section geometry of the macroscopic preform. Moreover, different ratios of GOS/SEBS composite fibers can be obtained by the thermal drawing technique, and the size of GOS can range from millimeters to nanometers.

As a proof of concept, a series of elastic fibers composed of GOS and SEBS matrix was first fabricated by thermal drawing. To obtain the bulk composite, a melt-blending process was adopted to mix the SEBS and GOS particles, and the obtained composite mixture was then hot-pressed into a rectangular preform. Next, the preform was thermally drawn into long fibers in a fiber drawing tower with a temperature range of 250–270 ℃. The composite preform has excellent thermoplasticity during the drawing process even

with a high content of GOS dopants (70 wt.%), and this can be ascribed to the large plasticity of SEBS. Notably, the high ratio of GOS in the SEBS matrix is beneficial for low-dose X-ray detection and imaging. The drawn elastic fibers are highly flexible and show bright photoluminescence when excited by a 254 nm UV light (Fig. 1c). In addition, the final fiber preserves the cross-section geometry of the preform due to the stable flow of the SEBS and GOS composite (Fig. 1d). The element mapping in fiber is characterized and shown in Fig. S1–7, confirming that GOS particles maintain their homogeneous distribution during the viscous flow from preform to fiber (Fig. 1e).

The stretchability of the drawn fibers loaded with different ratio of GOS was then characterized, as illustrated in Fig. 1f. The stress–strain curves indicate that the maximum strain of the drawn fiber shows a trend of rising and then declining with the increase in the GOS content from 0 to 70 wt.%, and the fiber can sustain strains up to 765% (with 2 wt.% GOS). These results indicate that the introduction of GOS particles into the SEBS does not deteriorate its elasticity (Movie S1–2). Specifically, an appropriate amount of GOS is beneficial to improve the elasticity of the SEBS matrix, and this condition may be related to the degree of crosslinking of the composite, including the density of the crosslinking point (Fig. S8). Furthermore, the drawn fiber shows excellent elasticity even with a high content of GOS (70 wt.%), as illustrated in Fig. 1g. The first stretch cycle shows the tensile characteristics with obviously higher modulus than the second stretch, which presents the obvious elastic behavior of rubber. This condition may be related to the rupture of the polystyrene (PS) phase and the formation of more elastic consolidation points during the stretch of the SEBS matrix. In addition, the composite has good resilience, and the initial modulus is significantly reduced. The excellent elastic properties of the drawn fibers are favorable for further construction of flexible fabrics for wearable applications.

Physical Mechanism of the Origin of Thermoplasticity of Fibers

To explore the origin of thermoplasticity, we first studied the rheological properties, including the storage modulus, the loss modulus, and the complex viscosity, of the pure SEBS and SEBS loaded with GOS, as illustrated in Fig. 2a–c. For both the pure SEBS fiber and SEBS fiber loaded with GOS, the storage modulus decreases rapidly, while the loss modulus and complex viscosity change slowly when the temperature exceeds 200 ℃. The rapid decrease of the storage modulus is a manifestation of the viscous flow of the SEBS, which well explains the excellent thermoplasticity during the thermal drawing process. The loss modulus and complex viscosity changed slowly, which indicates that the intermolecular

interactions of the SEBS are not drastically decreased by the increased temperature, which is crucial for the SEBS to withstand the drawing force and avoid the melt fracture. The addition of GOS can increase the moduli and viscosity, but does not affect the variation of the moduli or viscosity with the temperature. Specifically, when the GOS content is lower than 50 wt.%, the GOS particles have little effect on the modulus and viscosity of the composite (Fig. 2d–f), whereas the influence is significant when the GOS content exceeds 50 wt.%.

We further calculated the viscous flow activation energy (ΔE) of the SEBS composite loaded with different GOS. According to the Arrhenius equation [33], the relation between the viscosity (η) and the temperature (T) can be presented as follows:

$$\eta = Ae^{\Delta E/RT}, \tag{1}$$

where A and R are constants. From this equation, the activation energy of the SEBS composite with various GOS is calculated, as shown in Table 1. The GOS content has little influence on the viscous flow activation energy of the SEBS composite. This finding reveals that the addition of GOS has a negligible effect on the molecule motion of the SEBS composites. Hence, the doping of GOS in the SEBS matrix does not deteriorate the thermoplasticity and elasticity of the composite, making it suitable for thermal drawing and preserving the elasticity after the thermal drawing process.

Physical Mechanism of the Origin of Elasticity of Fibers

The microstructure of the pure SEBS and SEBS loaded with GOS was characterized by WAXS. As illustrated in Fig. 2g, the diffraction patterns show no obvious orientation in the preform, and the drawn fiber (loaded with 0.5 wt.% and 2 wt.% GOS) can be observed. This finding indicates that the orientation of the SEBS was already relaxed in the thermal drawing process, which is reasonable considering that the drawing speed (1 mm min^{-1}) utilized in this study is not high and the viscous flow of the SEBS is above 200 ℃, as revealed by the rheological properties. The diffraction curve of the preform and fiber (Fig. 2h–i) indicates that the composition of the material is not changed, and the broad peak ($q = 1.35$ Å^{-1}) and the sharp peak belong to the characteristic peak of SEBS and GOS, respectively. These results indicate that the composition and the structure of the SEBS composite remain unchanged after thermal drawing, thus contributing to the excellent elasticity after thermal drawing.
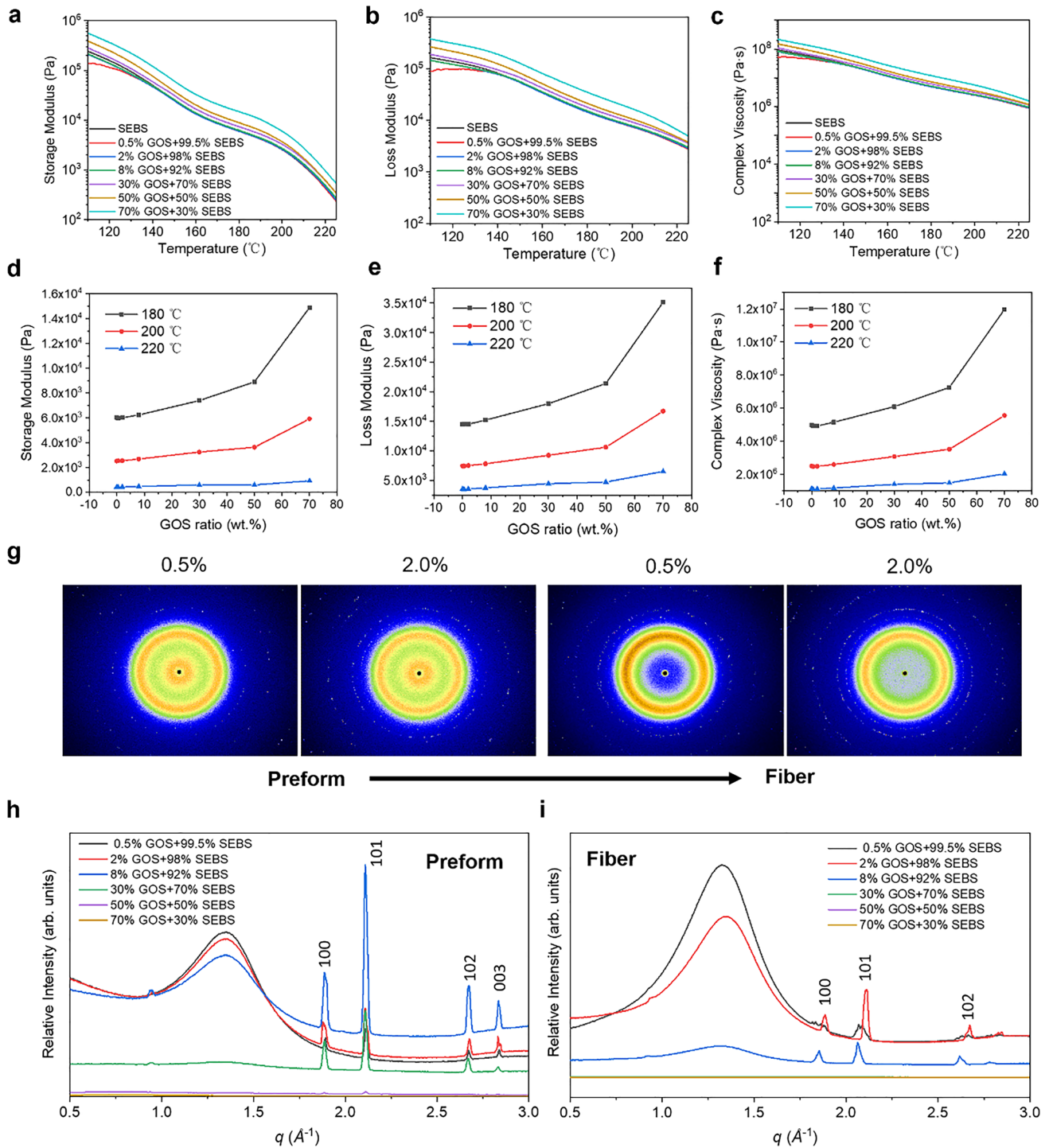
Fig. 2 Microstructure and rheological properties of the elastic fiber. **a–c** Storage modulus, loss modulus, and complex viscosity of the elastic fiber as a function of temperature, respectively. **d–f** Storage modulus, loss modulus, and complex viscosity of the elastic fiber loaded with different GOS at 180 ℃, 200 ℃, and 220 ℃, respectively. **g** WAXS patterns of the elastic preform and the drawn fiber loaded with 0.5 and 2 wt.% GOS, respectively. **h–i** WAXS profiles of the preform and the drawn elastic fiber loaded with various ratios of GOS

Table 1 Viscous flow activation energy of SEBS composite loaded with different GOS

GOS ratio (wt.%)	0	0.5	2	8	30	50	70
ΔE (KJ/mol)	61.68	61.58	60.95	61.17	61.01	64.71	68.56

Radiation Detection Properties of the Fabricated Super-elastic Fibers

The interaction between the radiation and the elastic fibers was studied. Generally, the radiation detection process includes radiation-harvesting and photons' generation. We first studied the radiation-harvesting performance of the elastic fiber loaded with various GOS, as illustrated in Fig. 3a. On the basis of the photon cross-sectional database, we can obtain that the absorption coefficient of the scintillator GOS is much higher than that of the commercial single crystal Si and the SEBS matrix over a broad range of photon energy from 0.001 MeV to 10 MeV. The detail radiation-harvesting process of a single elastic fiber (with a width of 1 mm and thickness of 0.5 mm) was theoretically simulated using Monte Carlo simulation (Fig. 3b). The simulated results show that the total energy deposition of the elastic fiber shows an increasing trend as the GOS activator increases from 0 to 99 wt.% (Fig. 3c), demonstrating that increasing the GOS content can greatly improve the radiation detection efficiency of the elastic fiber. The specific distribution of the energy deposition in the elastic fiber loaded with different GOS is shown in Fig. 3d. The total energy deposition of the elastic fiber with 70 wt.% GOS is 124 times that of the fiber with 0.5 wt.% GOS, confirming that the energy deposition increases with the enhancement of scintillator content. Thus, SEBS fibers loaded with various GOS can be designed for various applications. For example, the elastic fiber with high GOS content can be used for high-sensitivity, low-dosage X-ray detection, and imaging, while the elastic fiber with low GOS content can be used for wearable radiation detection.
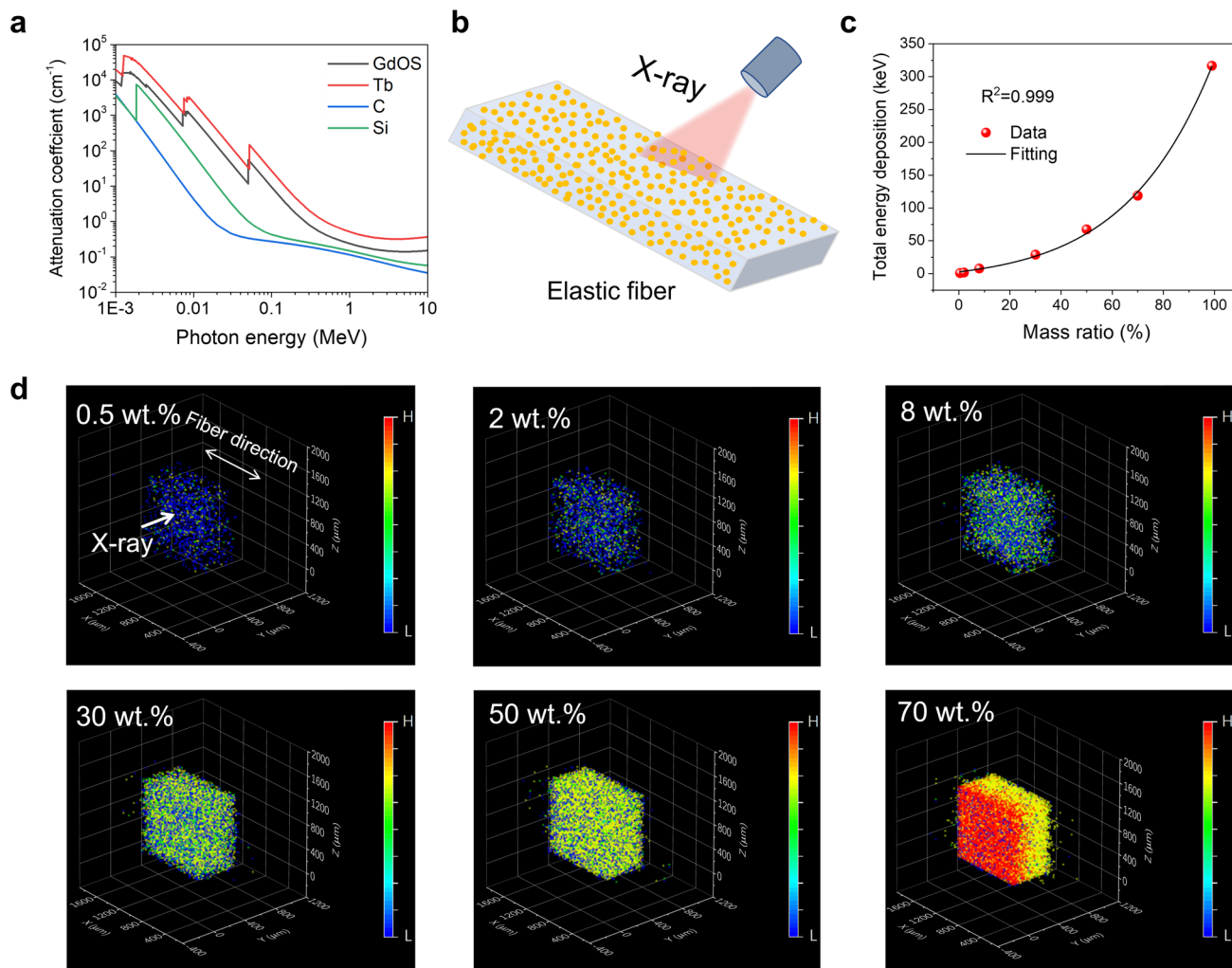

Fig. 3 Theoretical simulation of the interaction between radiation and the elastic fiber. a Absorption coefficients of various components of the elastic fiber and the commercial Si as a function of the photon energy of X-ray. b Image of a single elastic fiber irradiated by X-ray. c Relation of the total energy deposition with the content of the GOS scintillator. d Spatial distribution of the deposited energy in a single elastic fiber loaded with various GOS contents. The energy of the X-ray is 40 kV

The radioluminescence of the single elastic fiber (load with 70 wt.% GOS) was then experimentally evaluated using a 40 kV X-ray source. As shown in Fig. 4a, a set of intense emission bands can be clearly observed, which correspond to $^5D_4 \rightarrow {}^7F_3$ (622 nm), $^5D_4 \rightarrow {}^7F_4$ (587 nm), $^5D_4 \rightarrow {}^7F_5$ (546 nm), and $^5D_4 \rightarrow {}^7F_6$ (491 nm) electronic transitions of Tb^{3+}. When the dose rate of the X-ray source is increased,

the radioluminescence intensity of these elastic fibers can be gradually improved. Intriguingly, the radioluminescence intensity (such as at 546 nm) exhibits an excellent linear relationship with the X-ray dosage (as shown in the inset of Fig. 4a), demonstrating its great potential for X-ray dose indication. The dynamic response of the radioluminescence of the elastic fiber was further studied (Fig. S9). When the
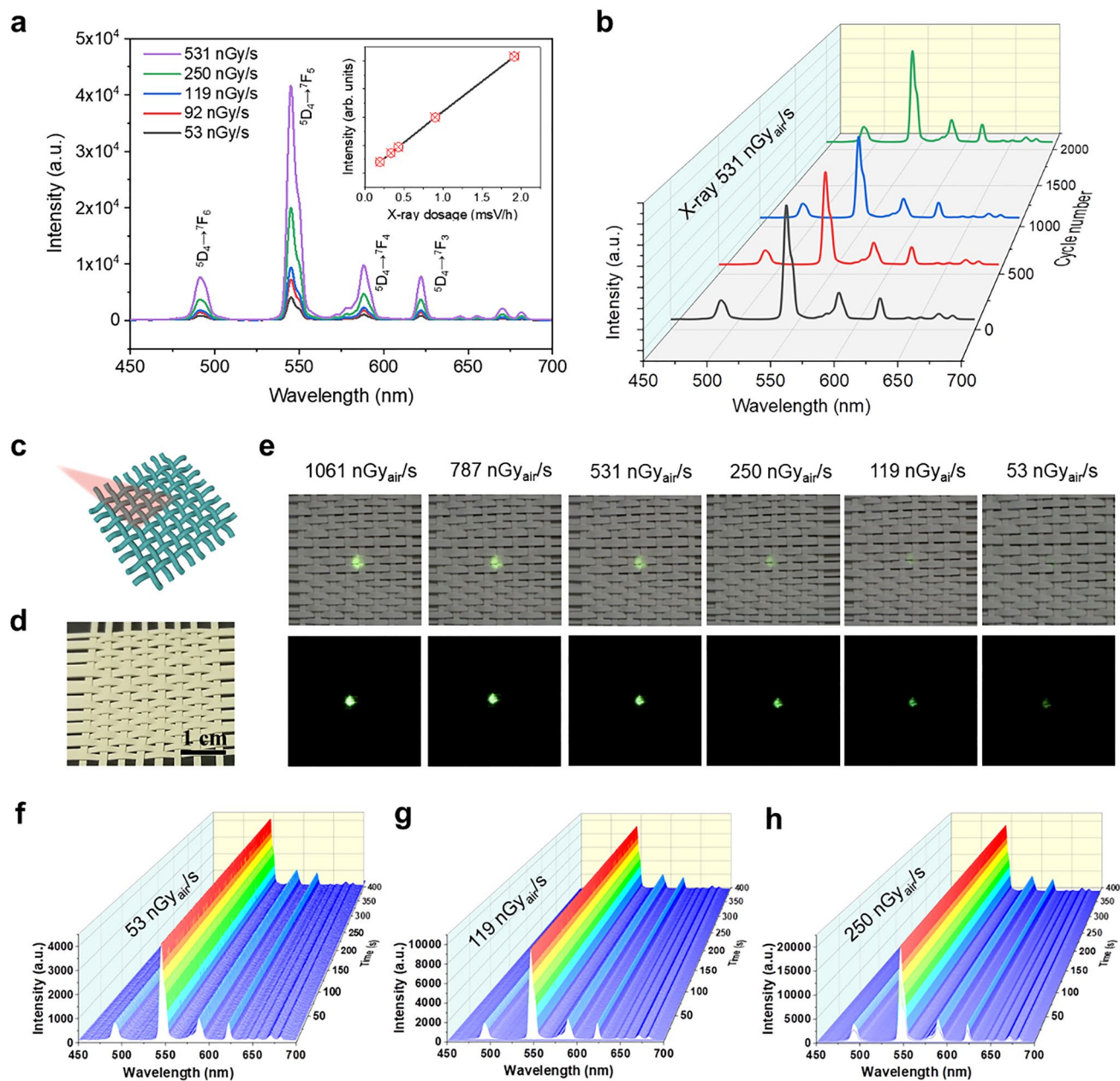
Fig. 4 Radiation detection response of the drawn elastic fibers. **a** Radioluminescence of the elastic fibers when irradiated with the X-ray dosage from 53 $nGy_{air}s^{-1}$ to 531 $nGy_{air}s^{-1}$. The inset is the relationship between the radioluminescence intensity (at 546 nm) and the X-ray dose rates. **b** Stability of the elastic fibers under various stretching cycles at a 100% elongation. **c** Schematic of a fabric irradiated with the X-ray. **d** Elastic fabric hand-knitted by the drawn elastic fibers. **e** Radioluminescence of a fabric in bright and dark environments with various X-ray dose rates. **f–h** Relation between the radioluminescence intensity of the elastic fabric and the irradiation time of X-rays with dosages of 53 $nGy_{air}s^{-1}$, 119 $nGy_{air}s^{-1}$, and 250 $nGyair s^{-1}$

X-ray dose rates increase from 53 to 531 $nGy_{air} s^{-1}$, the luminescence intensity of the elastic fiber increases rapidly, whereas it remains essentially unchanged at a fixed X-ray dosage, thus confirming the excellent stability and high sensitivity of the drawn elastic fiber. The impact of the repetitive deformation on the radioluminescence of the elastic fibers was assessed, as illustrated in Fig. 4b. The magnitude of the radioluminescence intensity does not show obvious changes after 2,000 cycles at a 100% elongation, demonstrating the high stability and reliability of the drawn elastic fibers for radiation detection.

The outstanding radiation detection properties of the elastic fibers prompted us to explore its applications for wearable and visual radiation detection. For this purpose, a piece of elastic fabric was hand-knitted using the drawn SEBS elastic fiber loaded with 70 wt.% GOS (with a width of ~ 500 μm and thickness of ~ 400 μm), as illustrated in Fig. 4c–d. The obtained fabric has strong radioluminescence in bright and dark environments when irradiated with X-rays with various dosages. More importantly, the radioluminescence intensity enhances with the increase in the X-ray dose rates (Fig. 4e), whereas it remains unchanged with the extension of irradiation time (Fig. 4f–h), thereby demonstrating that the elastic fabric can be used for long-term and stable visual X-ray detection and X-ray dose indication.

## Fabrication of Large-Area Elastic Fabric and Its Application

A large-area fabric with radiation detection was produced by the melt-spinning methods, as shown in Fig. 5a–b. We demonstrated two kinds of fabrics for visual radiation detection, including stretchable fabric (the main matrix is SEBS) and non-stretchable fabric (the main matrix is crystalline PP). These fabrics were manufactured from the obtained stretchable yarns and nonwoven fabrics (Figs. 5c–d and S10), and they both show bright luminescence in bright and dark environments upon irradiation with X-rays (Figs. 5e–f). These results indicate that the crystalline structure of the PP has little effect on the radioluminescence of the final elastic fabric. Notably, the manufactured fabrics have excellent stretching ability and washability (Fig. S11), and they can be used for wearable and visual radiation detection in various scenes. For example, when patients undergo a computed tomography scan, the fabrics can be attached to their clothes before they enter the examination room. When X-ray is turned on, the fabrics can show bright luminescence and detect the dosage of the X-rays (Fig. 5g). Another example is that the elastic fabrics can be woven into the sleeve of protective gear to show the X-ray dosage of the environment (Fig. 5h). Thus, these elastic fabrics are believed to have great potential for large-area wearable and visual radiation detection.

Except for visual radiation detection, flexible X-ray imaging is another application of the elastic fabrics. The imaging process is shown in Fig. 6a. Generally, the formation of X-ray imaging needs to meet three conditions [34]. First, X-ray has a certain penetration ability and can penetrate the sample to be tested. Second, due to the difference in density and thickness of the penetrated sample, the absorbed energy of X-ray in the process of penetration is different, which is why the energy of X-ray that passes through is different. Third, the X-ray penetrating the sample is invisible, and it can stimulate scintillation to produce fluorescence. The X-rays with different energy can cause a different luminescence intensity, which can be collected by the camera for radiation imaging of the sample. A metallic spring encapsulated in a pen was used for X-ray imaging with two types of fabrics (Fig. 6b). Figure 6c shows the X-ray images recorded using nonwoven PP with different exposure times. The profile of the metallic spring can be clearly observed. Figure 6d presents the X-ray images recorded by the woven SEBS fabric using the drawn elastic fibers. Compared with the nonwoven PP, the clear profile of the metallic spring has a shorter exposure time (0.2 s), which is ascribed to the high GOS content (70 wt.%) in SEBS composite fibers. The GOS content in PP fibers is only 2 wt.%. These results demonstrate that the manufactured scintillating fabrics can be used for flexible X-ray imaging, thus having great potential applications in large-area and flexible X-ray imaging.

Conclusions

In summary, we have described the principles, materials, and mechanism leading to the realization of super-elastic fibers and fabrics for efficient and visual radiation detection and imaging. Specifically, SEBS was selected as matrix due to its high stretchability, excellent thermoplasticity, UV stability, and aging resistance. The scintillator GOS was selected as the activator because of its excellent radiation absorption capacities and outstanding luminescent properties. Moreover, GOS has a short lifetime of only 1 ms, which is very sensitive for radiation detection and X-ray imaging.

Once the constituent materials were identified, the elastic scintillating fibers and fabrics can be manufactured using thermal drawing, melt-spinning, and spun-bond nonwoven technique. The advantages of thermal drawing can be summarized as follows: (1) The architectures of the final fiber can be rationally designed, which is dependent on the structure of the macroscopic preform. (2) A single preform can yield extremely long and uniform fibers with the same cross-section geometry of the macroscopic preform. (3) The diameter or thickness of the fiber can be controlled precisely from macro- to micro-scale. (4) Different ratios of GOS/ SEBS composite fibers can be obtained, and the addition of
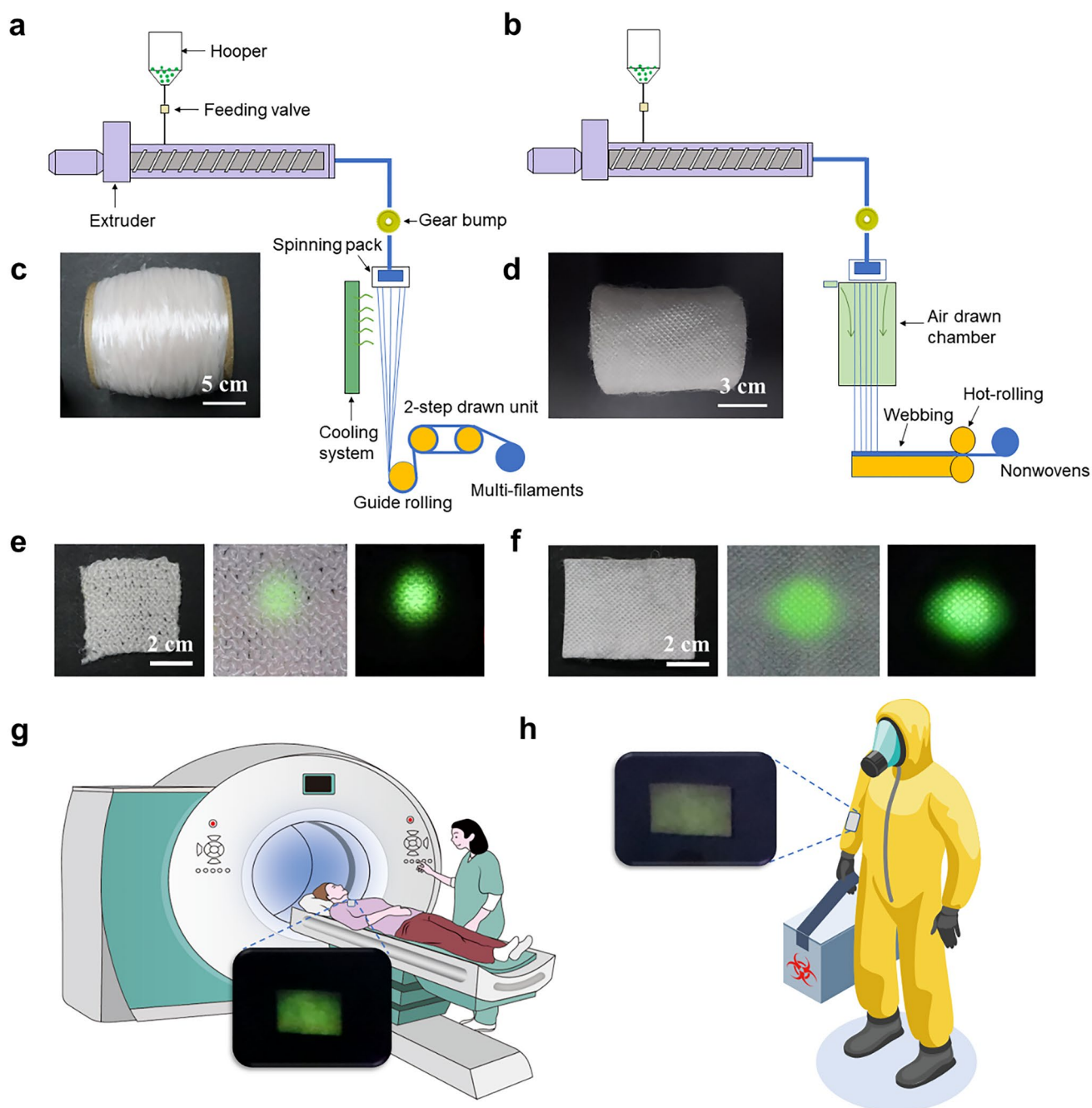
Fig. 5 Fabrication and visual radiation detection applications of the elastic fabrics. **a–b** Schematic assembly of multi-filament melt-spinning and spun-bonded nonwoven unit. **c–d** Pictures of stretchable SEBS yarns and nonwovens. **e–f** Pictures of stretchable SEBS yarns and nonwovens when they were irradiated by X-rays in bright and dark environments, respectively. **g–h** Two representative application scenes of the manufactured scintillating fabrics

GOS can reach 70 wt.%. The size of GOS can range from millimeter to nanometer scale. The advantages of the melt-spinning technique can be summarized as follows: (1) The elastic fibers and fabrics can be produced on an industrial scale for wearable applications. (2) The diameter of the final fiber can be controlled precisely from macro- to micro-scale. The main advantage of the spun-bond nonwoven process is that it is easy to realize large-scale production directly without environmental pollution.

On the basis of the above rules and considerations, we fabricated elastic fibers that can sustain strains up to 765% with an X-ray detection limit of as low as 53 $nGy_{air}\ s^{-1}$. Microstructure evolution, rheological properties, and Monte Carlo simulation results reveal that the drawn
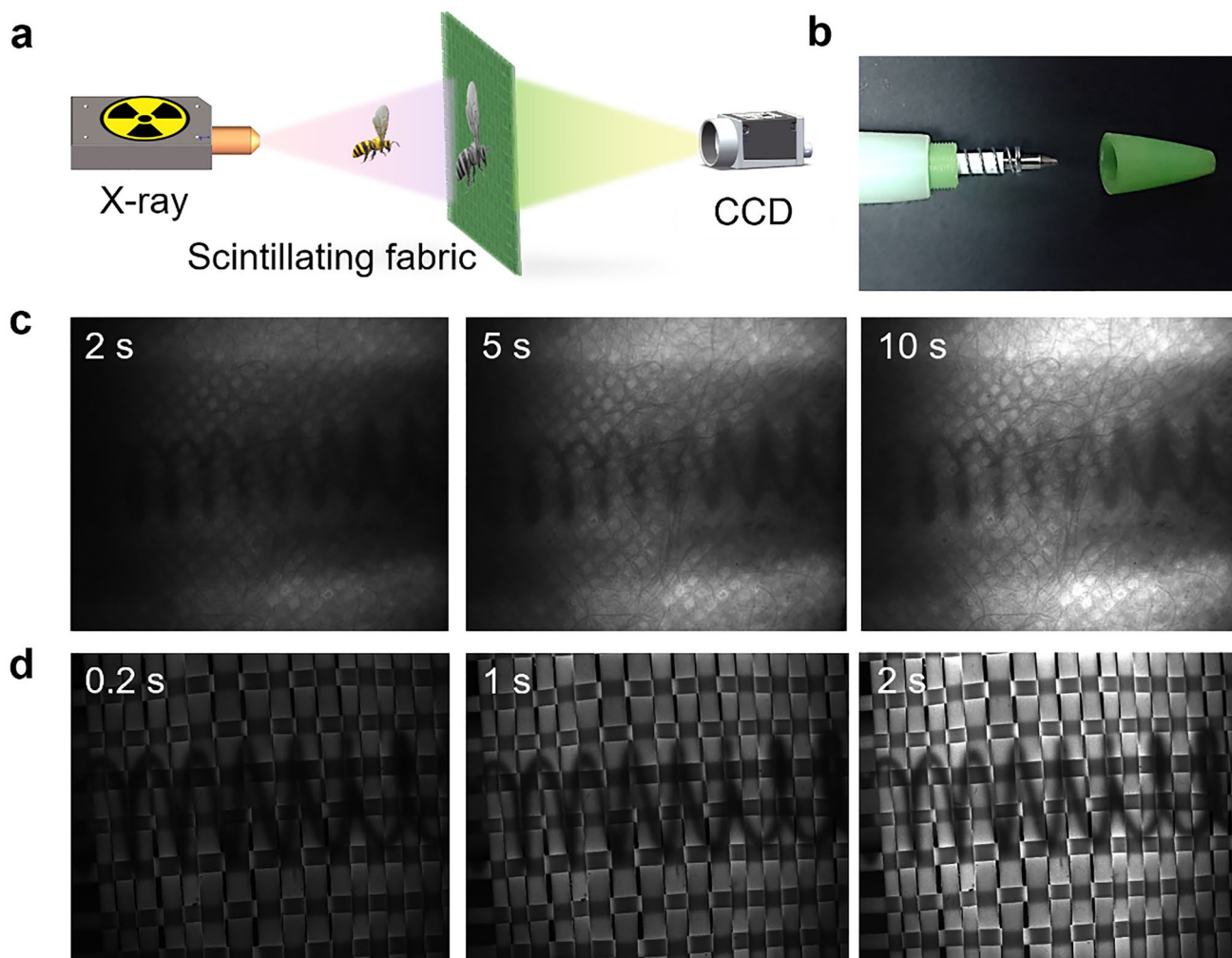
Fig. 6 Imaging application of the fabricated scintillating fabrics. **a** Schematic of the X-ray imaging process. **b** Image of a pen embedded with a metallic spring used for X-ray imaging. **c–d** X-ray imaging of the encapsulated metallic spring with different exposure times by nonwovens and stretchable SEBS yarns

elastic fiber has excellent thermoplasticity, elasticity, and radiation detection ability. The large area of stretchable fabrics for visual radiation detection and imaging was also demonstrated based on the outstanding radiation detection performance of the single elastic fiber. Furthermore, flexible radiation imaging application of the fabricated scintillating fabrics was realized. Our work not only provides super-elastic fibers and fabrics for visual radiation detection but also paves the way for the construction of next-generation stretchable fibers with multiple functions, which have promising applications in smart fabrics, medical monitoring, and flexible X-ray imaging, among others.

Supplementary Information The online version contains supplementary material available at https://doi.org/10.1007/s42765-023-00290-8.

Data availability The data that support the findings of this study are available from the corresponding authors upon request.

Declarations

Conflict of Interest The authors state that there are no conflicts of interest to disclose.

Open Access This article is licensed under a Creative Commons Attribution 4.0 International License, which permits use, sharing, adaptation, distribution and reproduction in any medium or format, as long as you give appropriate credit to the original author(s) and the source, provide a link to the Creative Commons licence, and indicate if changes were made. The images or other third party material in this article are included in the article's Creative Commons licence, unless indicated otherwise in a credit line to the material. If material is not included in the article's Creative Commons licence and your intended use is not permitted by statutory regulation or exceeds the permitted use, you will need to obtain permission directly from the copyright holder. To view a copy of this licence, visit http://creativecommons.org/licenses/by/4.0/.

References

1. Cui Y, Yao H, Zhang J, Zhang T, Wang Y, Hong L, Hou J. Over 16% efficiency organic photovoltaic cells enabled by a chlorinated acceptor with increased open-circuit voltages. *Nat Commun*. **2019**;*10*:2515.
2. Marques L, Vale A, Vaz P. State-of-the-art mobile radiation detection systems for different scenarios. *Sensors*. **2021**;*21*:1051.
3. Clinckemalie L, Valli D, Roeffaers M, Hofkens J, Pradhan B, Debroye E. Challenges and opportunities for CsPbBr$_3$ perovskites in low-and high-energy radiation detection. *ACS Energy Lett*. **2021**;*6*:1290.
4. Kong B, Wang E, Lu W, Li Z. Application of electromagnetic radiation detection in high-temperature anomalous areas experiencing coalfield fires. *Energy*. **2019**;*189*: 116144.
5. Yang T, Li F, Zheng R. Recent advances in radiation detection technologies enabled by metal-halide perovskites. *Mater Adv*. **2021**;*2*:6744.
6. McGregor D, Shultis J. Radiation detection: concepts, methods, and devices. CRC Press; 2020.
7. Brooks F, Hofstadter R. Scintillation counter. *Acc Science* **2020**.
8. Li Y, Shao W, Chen L, Chen L, Wang J, Nie J, Zhang H. Lead-halide Cs$_4$PbBr$_6$ single crystals for high-sensitivity radiation detection. *NPG Asia Mater*. **2021**;*13*:40.
9. Liang H, Cui S, Su R, Guan P, He Y, Yang L, Du X. Flexible X-ray detectors based on amorphous Ga$_2$O$_3$ thin films. *ACS Photonics*. **2018**;*6*:351.
10. Johns P, Nino J. Room temperature semiconductor detectors for nuclear security. *J Appl Phys*. **2019**;*126*: 040902.
11. Büchele P, Richter M, Tedde SF, Matt GJ, Ankah GN, Fischer R, Schmidt O. X-ray imaging with scintillator-sensitized hybrid organic photodetectors. *Nat Photonics*. **2015**;*9*:843.
12. Kasap S, Frey J, Belev G, Tousignant O, Mani H, Greenspan J, Rowlands JA. Amorphous and polycrystalline photoconductors for direct conversion flat panel X-ray image sensors. *Sensors*. **2011**;*11*:5112.
13. Eden A, Morton E, De Antonis P. Thin-film CdTe for imaging detector applications. *Nucl Instrum Meth Phys Res Sect A*. **2001**;*458*:7.
14. Szeles C. CdZnTe and CdTe materials for X-ray and gamma ray radiation detector applications. *Phys Status Solidi (b)*. **2004**;*241*:783.
15. Street R, Ready S, Lemmi F, Shah K, Bennett P, Dmitriyev Y. Electronic transport in polycrystalline PbI$_2$ films. *J Appl Phys*. **1999**;*86*:2660.
16. Lin Z, Lv S, Yang Z, Qiu J, Zhou S. Structured scintillators for efficient radiation detection. *Adv Sci*. **2022**;*9*:2102439.
17. Blasse G. Scintillator materials. *Chem Mater*. **1994**;*6*:1465.
18. Ma W, Jiang T, Yang Z, Zhang H, Su Y, Chen Z, Yang Y. Highly resolved and robust dynamic X-ray imaging using perovskite glass-ceramic scintillator with reduced light scattering. *Adv Sci*. **2021**;*8*:2003728.
19. Gektin A, Korzhik M. Inorganic scintillators for detector systems. Springer; 2017.
20. Rodnyi P. Physical processes in inorganic scintillators. CRC Press; 1997.
21. Ginther R. New cerium activated scintillating glasses. *Ire T Nucl Sci*. **1960**;*7*:28.
22. Shi Z, Lv S, Tang G, Tang J, Jing L, Qian Q, Zhou S, Yang Z. Hybridized oxyfluoride photonic glasses for radiation detection. *ACS Appl Mater Inter*. **2020**;*12*:17752.
23. Drake D, Nilsson L, Faucett J. Bismuth germanate scintillators as detectors for high-energy gamma radiation. *Nucl Instrum Meth Phys Res*. **1981**;*188*:313.
24. Nestor O, Huang C. Bismuth germanate: a high-Z gamma-ray and charged particle detector. *IEEE T Nucl Sci*. **1975**;*22*:8.
25. Brooks F. Development of organic scintillators. *Nucl Instrum Methods*. **1979**;*162*:477.
26. Horrocks D. Applications of liquid scintillation counting. Elsevier; 2012.
27. Yan W, Page A, Nguyen-Dang T, Qu Y, Sordo F, Wei L, Sorin F. Advanced multimaterial electronic and optoelectronic fibers and textiles. *Adv Mater*. **2019**;*31*:1802348.
28. Yan W, Dong C, Xiang Y, Jiang S, Leber A, Loke G, Tao G. Thermally drawn advanced functional fibers: new frontier of flexible electronics. *Mater Today*. **2020**;*35*:168.
29. Loke G, Yan W, Khudiyev T, Noel G, Fink Y. Recent progress and perspectives of thermally drawn multimaterial fiber electronics. *Adv Mater*. **2020**;*32*:1904911.
30. Qu Y, Nguyen-Dang T, Page A, Yan W, Das Gupta T, Rotaru G, Sorin F. Superelastic multimaterial electronic and photonic fibers and devices via thermal drawing. *Adv Mater*. **2018**;*30*:1707251.
31. Chen L, Wu Y, Huo H, Tang B, Ma X, Wang J, Zhou S. Nanoscale Gd$_2$O$_2$S: Tb scintillators for high-resolution fluorescent imaging of cold neutrons. *ACS Appl Nano Mater*. **2022**;*5*:8440.
32. Kim J, Cha B, Bae J, Lee C, Kim H, Chang S, Kim T. Fabrication and characterization of pixelated Gd$_2$O$_2$S: Tb scintillator screens for digital X-ray imaging applications. *Nucl Instrum Meth Phys Res Sect A*. **2011**;*633*:S303.
33. Vyazovkin S. Activation energies and temperature dependencies of the rates of crystallization and melting of polymers. *Polymers*. **2020**;*12*:1070.
34. Martz H, Logan C, Schneberk D, Shull P. X-ray Imaging: fundamentals, industrial techniques and applications. CRC Press; 2016.